HHS Public Access

Author manuscript

Nature. Author manuscript; available in PMC 2017 June 21.

Published in final edited form as:

Nature. 2016 August 04; 536(7614): 76–80. doi:10.1038/nature18944.

A novel excitatory network for the control of breathing

Tatiana M. Anderson[1,2,*], **Alfredo J. Garcia III**[1,*], **Nathan A. Baertsch**[1], **Julia Pollak**[1], **Jacob C. Bloom**[1], **Aguan D. Wei**[1], **Karan G. Rai**[1], and **Jan-Marino Ramirez**[1,3,†]

[1]Seattle Children's Research Institute, Center for Integrative Brain Research, Seattle, WA, USA

[2]University of Washington School of Medicine, Graduate Program for Neuroscience, Seattle, WA, USA

[3]University of Washington School of Medicine, Department of Neurological Surgery and Pediatrics, Seattle, WA, USA

Abstract

Breathing must be tightly coordinated with other behaviors such as vocalization, swallowing, and coughing. These behaviors occur after inspiration, during a respiratory phase termed postinspiration[1]. Failure to coordinate postinspiration with inspiration can result in aspiration pneumonia, the leading cause of death in Alzheimer's disease, Parkinson's disease, dementia, and other neurodegenerative diseases[2]. Here we describe an excitatory network that generates the neuronal correlate for postinspiratory activity. Glutamatergic-cholinergic neurons form the basis of this network, while GABAergic inhibition establishes the timing and coordination with inspiration. We refer to this novel network as the postinspiratory complex (PiCo). PiCo has autonomous rhythm generating properties and is necessary and sufficient for postinspiratory activity in vivo. PiCo also has distinct responses to neuromodulators when compared with other excitatory brainstem networks. Based on the discovery of PiCo we propose that each of the three phases of breathing is generated by a distinct excitatory network: The preBötzinger complex, which has been linked to inspiration[3,4], the PiCo as described here for the neuronal control of postinspiration, and the Lateral parafacial region (pF_L) which has been associated with active expiration, a respiratory phase recruited during high metabolic demand[4,5].

Neurons in phase with postinspiratory activity have previously been identified in the Bötzinger Complex (BötC), a region that is primarily inhibitory[6, 7]. However, the source of excitation that drives this inhibitory network is not well-defined. Here we identified the

†Correspondence to: Jan-Marino Ramirez; nino1@uw.edu.
*These authors contributed equally to this work
Correspondence and requests for materials should be addressed to J-M.R. (nino1@uw.edu).

Author Contributions:

T.A, A.G, and J-M.R. designed all experiments. T.A., A.G., N.B, J.P., J.B., A.W., and K.R. performed the experiments. T.A., A.G., N.B, and J.P. analyzed the data. T.A., A.G., N.B, J.P., and J-M.R. contributed to manuscript preparation. T.A. and J-M.R wrote the manuscript.

The authors declare no competing financial interests.

Readers are welcome to comment on the online version of this article at www.nature.com/nature.

location and neurochemical phenotype of an excitatory and rhythmogenic neuronal population that is specifically active during postinspiration.

We developed a horizontal slice preparation in postnatal day (P)5–10 mice that captures the ventral extent of the medulla, including the ventral respiratory column[8] (VRC, Fig. 1a, Extended Data Fig. 1), and recorded extracellular, bilaterally-synchronized respiratory rhythmic population activity. Inspiratory population activity was identified within the pre-Bötzinger complex (preBötC[9], Fig. 1a), a network that is necessary and sufficient for generating inspiration[3,10]. Horizontal slices also generated postinspiratory population activity that: (a) discharged immediately following, but never during, inspiratory activity, and (b) followed sighs generated in the preBötC[11] (Fig. 1a).

Postinspiratory bursts spontaneously occurred on average after 1 of 12 preBötC bursts (Fig. 1a, Extended Data Fig. 2). This decreased excitability could be due to the absence of the pons, which provides descending neuromodulatory input, including norepinephrine (NE) [12]. Indeed, postinspiratory activity was exquisitely sensitive to NE. In 2 μM NE postinspiratory population activity occurred with nearly every inspiratory cycle (Fig. 1a, Extended Data Fig. 2). Therefore, we used this NE concentration as a tool to facilitate postinspiratory activity in vitro.

Postinspiratory population activity was most pronounced approximately 400 μm rostral to the preBötC, dorsal to the BötC, and caudal to the facial (VII) nucleus. We refer to this area as the Postinspiratory Complex (PiCo, Fig. 1a; Extended Data Fig. 1). To assess the distribution of postinspiratory activity, we positioned one electrode in the PiCo region and a second electrode contralaterally to map the amplitude of postinspiratory population activity across the VRC (Fig. 1a). Postinspiratory activity was concentrated rostral to the preBötC, but extended caudally and partially overlapped with inspiratory activity.

PiCo was anatomically characterized by immunohistological labeling of transverse sections (Fig. 1b1) revealing that ChAT (choline acetyltransferase)-positive cholinergic and Vglut2 (vesicular glutamate transporter 2)-expressing glutamatergic neurons in the *Vglut2*-cre;Ai6 mouse co-localized in PiCo, dorsomedial to Nucleus ambiguus (NA) (Fig. 1b1–b3). In contrast, ChAT-positive neurons in NA lacked substantial Vglut2 expression (Extended Data Fig. 3). In the sagittal plane, ChAT and Vglut2 co-labeled PiCo neurons were located dorsal and caudal to the VII nucleus (Fig. 1c1). Quantifying ChAT and Vglut2 co-expression revealed that PiCo mainly extends from 40 to 280 μm medial to the NA (Fig. 1c2) and −50 to 250 μm caudal to the VII nucleus caudal border (Fig. 1c3). In situ hybridization confirmed expression of *Vglut2* mRNA in *Chat*-derived PiCo neurons from transverse sections of *Chat*-cre;Ai14 mice (Fig. 1d,e).

The Cre-dependent reporter line Ai27, which conditionally expresses channelrhodopsin-2 (ChR2) fused to td-Tomato in the presence of a selective, promoter-driven Cre, allowed for photo-stimulation of specific neuronal sub-populations[13]. PiCo neurons were recorded from *Vglut2*-cre;Ai27 and *Chat*-cre;Ai27 horizontal slices. Membrane depolarization of tetrodotoxin (TTX) isolated PiCo neurons during light stimulation demonstrated that functionally identified postinspiratory cells were glutamatergic and cholinergic (Fig. 2a),

consistent with the histological results. PiCo neurons generated neither pre-inspiratory bursts nor a biphasic discharge typical of pre-inspiratory neurons in the retrotrapezoidal nucleus parafacial respiratory group (RTN/pFRG) region[14].

Postinspiratory population activity was unaffected by bath-applied strychnine to block glycinergic inhibition (Fig. 2b, Extended Data Fig. 4). However, PiCo and preBötC bursts progressively synchronized following blockade of GABAergic inhibition with gabazine, in the presence (Fig. 2b, Extended Data Fig. 5) or absence (data not shown) of strychnine. The burst area of postinspiratory activity was increased during the blockade of synaptic inhibition (Extended Data Fig. 4), indicating that the PiCo rhythm is modulated, but not generated, by inhibitory mechanisms. Inspiratory and postinspiratory bursts persisted following NMDA receptor blockade (CPP, data not shown), while bursting was abolished following non-NMDA glutamatergic blockade (CNQX, Fig. 2b). We conclude that inspiratory and postinspiratory activities are generated by glutamatergic, non-NMDA dependent mechanisms, while the timing of inspiratory and postinspiratory bursts is established by GABAergic mechanisms.

Inspiratory rhythm generating neurons in the preBötC are derived from Dbx1 expressing progenitor cells[15]. To explore whether these neurons interact with PiCo, we utilized a tamoxifen inducible transgenic line (*Dbx1*-cre-ERT2;Ai27) in which *Dbx1*-positive cells born after embryonic day (E)10.5 express channelrhodopsin-2. Photo-stimulating preBötC neurons in horizontal slices from *Dbx1*-cre-ERT2;Ai27 animals inhibited all recorded PiCo neurons in 2 μM NE and in strychnine (Fig. 2c). In gabazine, this light-evoked inhibition was eliminated. The blockade of GABAergic inhibition revealed that PiCo neurons also received excitatory input from the preBötC, which was blocked by CNQX (Fig. 2c). Thus, inspiratory activity involving *Dbx1*-derived neurons concurrently excites and inhibits PiCo neurons via glutamatergic and GABAergic mechanisms, respectively; however, under normal conditions, GABAergic interactions dominate over the concurrent glutamatergic excitation from the preBötC (Fig. 2c).

Since PiCo neurons co-express acetylcholine and glutamate (Fig. 1), we tested whether the postinspiratory rhythm depends on cholinergic mechanisms. Atropine, a muscarinic receptor antagonist, but not mecamylamine, a nicotinic receptor antagonist, depressed postinspiratory burst frequency. However, postinspiratory bursting persisted in the presence of both blockers and returned to near baseline frequency by raising NE to 4 μM (Extended Data Fig. 6). Thus, PiCo rhythms are modulated by, but not dependent on, cholinergic mechanisms.

PiCo neurons were intrinsically sensitive to the μ-opioid receptor agonist DAMGO (Extended Data Fig. 7). In horizontal slices, PiCo population bursts were nearly eliminated by 25 nM DAMGO, whereas burst frequency in the preBötC was only slightly decreased (Fig. 2d, Extended Data Fig. 8). This exquisite opioid sensitivity unambiguously differentiates PiCo from the previously described RTN/pFRG, a region that is thought to contain the network generating active expiration[4] and known to be insensitive to μ-opioid receptor activation[16]. The peptide somatostatin (SST) had little effect on preBötC activity, but inhibited postinspiratory PiCo activity (Fig. 2e, Extended Data Fig. 8). These data are consistent with the inhibition of postinspiration in vivo[17].

Optogenetic stimulations of ChAT-positive neurons always elicited postinspiratory bursts recorded from PiCo in horizontal slices. These stimulations never evoked an inspiratory burst (Extended Data Fig. 9), nor burst activity in intracellularly recorded NA neurons (data not shown). Because of the specificity for postinspiratory activity, we utilized adult *Chat*-cre;Ai27 animals to stimulate PiCo in vivo. Similar to in vitro results, optogenetic activation of ChAT-positive neurons at the level of PiCo (Fig. 3a–c) reliably evoked bursts in the cervical vagal nerve (cVN) (Fig. 3d, Extended Data Fig. 9). Photo-evoked postinspiratory bursts delayed the subsequent inspiration (Fig. 3d,e, Extended Data Fig. 8). This delay was eliminated following bilateral injection of DAMGO into PiCo (Extended Data Fig. 10). Thus, postinspiration has a mutual inhibitory relationship with inspiratory activity.

To assess whether PiCo is responsible for generating postinspiratory motor output in vivo, we took advantage of PiCo's sensitivity to SST and DAMGO. Injecting SST or DAMGO bilaterally into PiCo in vivo (Fig. 3a–c) dramatically reduced spontaneous vagal postinspiratory burst duration and amplitude (Fig. 3f–h). Collectively, these results suggest that PiCo is both necessary and sufficient for generating postinspiratory activity.

Moreover, PiCo seems to possess autonomous rhythmogenic properties. In horizontal slices, NE concentrations above 2 μM generated ectopic PiCo population bursts that outpaced the preBötC rhythm (Fig. 4a, Extended Data Fig. 2). Ectopic bursts occurred in any phase of the inspiratory cycle except during preBötC bursts (Fig. 4b), consistent with photo-evoked PiCo bursts (Extended Data Fig. 9).

To further test the possibility that PiCo is an autonomous rhythm generator, we separated the VRC into two adjacent rostral and caudal transverse slices (Fig. 4c). Together, these slices span a total length of 1–1.1 mm of the rostrocaudal VRC beginning with the caudal portion of the VII nucleus. Recording from the caudal face of each transverse slice revealed a slower rhythm in the rostral transverse slice containing PiCo compared to the caudal slice containing the preBötC[3,11] (Fig. 4c). In 2 μM NE, both transverse slices exhibited regular rhythmic activities with similar burst frequencies (Fig. 4c, Extended Data Fig. 2) that persisted in the presence of strychnine, gabazine, and CPP, but were abolished in CNQX (Extended Data Fig. 4), resembling the findings in horizontal slices. Consistent with our histological characterizations, optogenetic stimulation of either *Vglut2*-cre;Ai27 or *Chat*-cre;Ai27 rostral slices evoked population bursts in PiCo (Fig. 4d). This provides additional evidence that glutamatergic/cholinergic neurons are important for rhythm generation within the PiCo network. Furthermore, PiCo activity was exquisitely sensitive to DAMGO and SST in isolated transverse slices (Extended Data Fig. 8). We conclude that PiCo and preBötC can function as independent oscillators with similar rhythm generating, but distinct modulatory properties.

As an excitatory rhythmogenic network, PiCo may not only be involved in the context of breathing, but might also contribute to the generation of other postinspiratory behaviors such as swallowing and vocalization. While behavioral assays were not performed in this study, various types of postinspiratory burst waveforms were observed in the vagal nerve (Extended Data Fig. 10) that were similarly affected by the manipulation of PiCo, supporting a potential broad role of this network in postinspiratory activities. In this context

it will be interesting to (a) resolve the role of PiCo in specific postinspiratory behaviors and (b) identify how PiCo interacts with other neural networks such as the Kolliker-Fuse Nucleus, a pontine structure that has been hypothesized to gate postinspiratory activity[18], and the periaqueductal gray, a structure involved in vocalization and the control of postinspiration[19].

Based on these results, we propose a triple oscillator model, wherein the three phases of breathing, inspiration, postinspiration, and active expiration, are generated by three spatially distinct excitatory rhythmogenic microcircuits, the preBötC, PiCo, and pF_L, respectively, which are temporally coordinated by inhibitory interactions. The existence of discrete excitatory networks may facilitate the differential and dynamic control of ventilatory and non-ventilatory behaviors. Coupled oscillators[20] have also been hypothesized for networks controlling locomotion[21], scratching[22], swimming[23] and the circadian clock[24]. Thus, this network organization may constitute a general principle of rhythm generation that promotes flexible control of complex biological processes.

Methods

Animals

All experiments were performed with the approval of the Institute of Animal Care and Use Committee of the Seattle Children's Research Institute. Mice were maintained with rodent diet and water available *ad libitum* in a vivarium with a 12 h light/dark cycle at 22°C. In this study, we utilized both CD1 Swiss mice and Cre reporter mice generated on a C57BL/6 background. Ai27 mice were bred to conditionally express Channelrhodopsin-2 (H134R) fused to tdTomato inserted in the *ROSA26* locus [B6.Cg–*Gt(ROSA)26Sor*$^{tm27.1(CAG-COP4*H134R/tdTomato)Hze}$/J; The Jackson Laboratory]. Ai6 mice were bred to express a green fluorescent protein ZsGreen1 inserted in the *ROSA*26 locus [B6.Gt(ROSA)26Sor$^{tm6(CAG-ZsGreen1)Hze}$; The Jackson Laboratory]. Similarly, Ai14 mice were bred to express a red fluorescent protein tdTomato inserted into the *ROSA*26 locus [Gt(ROSA)26Sor$^{tm14(CAG-tdTomato)Hze}$; The Jackson Laboratory]. Cre-driver mice expressed Cre recombinase under the control of subtype-specific promoters, including *Chat*-cre (B6;129S6–*Chat*$^{tm2(cre)Lowl}$/J; The Jackson Laboratory) and *Vglut2*-cre (B6;Slc17a6$^{tm2(cre)Lowl}$; Bradford Lowell). *Dbx1*-cre-ERT2 (*Dbx1*^{CreERT2}; [15,28]) dams were bred with Ai27 males and pregnancies were timed and monitored. We intraperitoneally injected tamoxifen [25 mg/kg; from 10 mg tamoxifen (Sigma-Aldrich) dissolved per mL of corn oil] on embryonic day (E)10.5. Mice were typically born after 20 days of gestation. No method of randomization was used to determine how animals were allocated to experimental groups and the investigators were not blinded when analyzing data in this study.

In Vitro Slice Preparations

We dissected the ventral respiratory column (VRC) using three types of brainstem slices: (1) A "caudal" transverse slice that contains the preBötC as previously described[3,11], (2) a rostral transverse slice that encompasses the BötC and caudal portions of the VII nucleus, and (3) a horizontal slice that bilaterally isolates the VRC extending from the VII nucleus to the spinal cord. Slices were obtained at postnatal day (P)5–10 from CD1 and transgenic

C57BL/6 mice. Animals were anesthetized via rapid hypothermia on ice before quick decapitation at spinal cervical level C4-C5. The three slices types were differentiated by the cutting angle, plane and thickness of the slice.

For transverse slices, the head was pinned in a tissue-culture dish filled with a silicone elastomer (Sylgard). Skin and connective tissues were removed, and fine scissors were used to cut along skull sutures to separate the interparietal region of the skull and expose the cerebellum. A one-sided razor was used to make a single cut between the inferior colliculus and cerebellum. The brainstem was isolated by removing the cerebellum in ice-cold, oxygenated (95% O_2, 5% CO_2) artificial cerebrospinal fluid (aCSF) containing (in mM): 128 NaCl, 3 KCl, 1.5 $CaCl_2$, 1 $MgCl_2$, 24 $NaHCO_3$, 0.5 NaH_2PO_4, and 30 D-glucose (pH 7.4, 305–312 mOSM). A slanted (~15° from vertical) agar block was secured on a specimen tray, and then the isolated brainstem and spinal cord preparation was glued with cyanoacrylate to the slanted portion of the agar such that the rostral end was facing upward and the dorsal side was glued to the agar. Serial transverse slices proceeded on a vibratome until visual landmarks became clear. Once the 4^{th} ventricle was completely open, a 550 μm slice was taken to obtain the rostral transverse slice containing PiCo. The caudal face of this slice was characterized by containing the rostral-most portion of the NA and the caudal portion of the VII nucleus. The subsequent 550 μm slice isolated the caudal transverse slice. This caudal slice was identical to the well-established transverse slice known to contain the preBötC[11]. From an individual animal we routinely obtained both the rostral and the caudal slice preparation and recorded from the caudal side of each of the transverse slices in the same recording chamber.

To obtain the third type of slice preparation, the horizontal slice, the brainstem was mounted as described for the transverse slices. Serial coronal slices were taken from the rostral end of the brainstem until the facial nerves became visible, approximately 800–1000 μm. The agar block was then removed from the specimen tray and reoriented so that the ventral surface of the brainstem faced upward and the blade advanced toward the rostral portion of brainstem. The preparation was angled so that the ventral-most portion of the medulla was approximately level with the ventral-most portion of the spinal cord. The blade was positioned level to the rostroventral edge of the brainstem, stepped 900 μm downward (in the dorsal direction), and a single horizontal slice was cut retaining the ventral portion of the brainstem and spinal cord. The horizontal slice preserves long-range bilateral network interactions throughout the rostral-caudal axis of the VRC.

In Vitro Electrophysiology

All slices were immediately transferred to the recording chamber, where they were superfused with aCSF at a rate of 10 mL/minute, bubbled continuously in carbogen (95% O_2 and 5% CO_2) to oxygenate and adjust pH to 7.4, and allowed to equilibrate to experimental temperature (33 ± 2 degrees Celsius, thermoneutral zone for mice). Population activity was obtained by raising the extracellular potassium concentration from 3 mM to 8 mM in two steps over 30 minutes. This is defined as “spontaneous conditions”.

Population activity was routinely recorded with borosilicate glass microelectrodes (World Precision Instrument) pulled on a Flaming/Brown micropipette puller (model P97, Sutter

Instrument Co., <1 MOhm tip resistance) that are placed on the slice surface. Signals were amplified, filtered, and integrated as previously published[25]. Automated burst analysis software was used to determine population recordings of burst frequency and amplitude[29].

The mapping experiment (Fig. 1a) was performed by placing a reference extracellular electrode upon PiCo and a second, mapping extracellular electrode on the contralateral side of a horizontal slice. The mapping electrode was systematically moved in 100 μm stereotaxic steps rostral, caudal, medial, and lateral to PiCo. Postinspiratory burst amplitudes from the mapping electrode were normalized to that from the reference electrode to create a heat map of activity.

In horizontal and rostral transverse slices from transgenic mice expressing ChR2 in a subset of neurons, PiCo (contralateral to the recording electrode) was light stimulated by using fiber optic (DPSSL Driver, blue 473 nm wavelength, 200 μm diameter, <22 mW/mm^2 intensity) for 500 ms or 1.5 s. Collections of 10 or 40 sweeps were recorded in succession (shown overlaid).

Intracellular blind patch recordings were performed on PiCo neurons. Borosilicate glass patch electrodes (with filaments, World Precision Instruments) were pulled (P-97 Flaming/Brown micropipette puller, Sutter Instrument Co.) to a 6–12 MΩ resistance. Electrodes were filled with an intracellular patch solution containing (in mM): 140 K-gluconic acid, 1 CaCl2, 10 EGTA, 2 MgCl2, 4 Na2ATP, 10 HEPES (pH = 7.4). Whole cell patch-clamp recordings were obtained in current clamp configuration using a Multiclamp 700B amplifier (Molecular Devices) sampling at 20 kHz. Extracellularly recorded signal was sampled at 1.67 kHz, amplified 10,000 times, filtered (low pass, 1.5 kHz; high pass, 250 Hz), rectified, and integrated using an electronic filter. Both extracellular and intracellular recordings were obtained with Clampex 10.0 (Molecular Devices). Recordings were stored on a computer for post-hoc analysis.

Receptor antagonists and neuromodulators were bath perfused during in vitro extracellular and intracellular recordings. All stock solutions were stored at −20°C in small-volume aliquots to avoid repetitive freezing and thawing. Strychnine (1 μM, glycine receptor antagonist, Sigma Aldrich) and SR 95531 hydrobromide (gabazine, $GABA_A$ receptor antagonist, 10 μM, Tocris) were used to block inhibitory synaptic transmission. To further block all fast synaptic transmission, 3-((±)2-carboxypiperazin-4yl)propyl-1-phosphate (CPP, NMDA receptor antagonist, 10 μM, Tocris) and 6-Cyano-7-nitroquinoxaline-2,3-dione (CNQX, AMPA receptor antagonist, 20 μM, Alimony Labs, diluted in DMSO) was bath applied. To block action potentials, 1 μM tetrodotoxin (TTX, Sigma-Aldrich) was used. To block cholinergic receptors, 10 μM atropine, a muscarinic receptor antagonist (Sigma-Aldrich) and 1 μM Mecamylamine hydrochloride, a nicotinic receptor antagonist (Sigma Aldrich) were bath applied. To stimulate the PiCo rhythm, DL-norephrine hydrochloride (NE, 1–4 μM, Sigma-Aldrich) was used; and to inhibit the PiCo rhythm, [D-Ala^2, N-Me-Phe^4, Gly^5-ol]-Enkephalin (DAMGO, 1–300 nM, Sigma-Aldrich) and Somatostatin (SST, 500 nM, Tocris) were applied.

In Vivo Electrophysiology

Adult mice were prepared as described previously[26]. *Chat*-cre;Ai27 mice (P)140–250 were anesthetized with urethane (1.5 g/kg), placed in a supine position, and the head was stabilized with ear bars. The trachea was exposed via a cervical midline incision and cannulated with a U-shaped tracheal tube. For the remainder of the surgery and experimental protocol, mice were allowed to spontaneously breathe humidified O_2 (FiO_2=100%). The rostral ends of the trachea and esophagus were removed, followed by removal of the muscle and bone covering the ventral brainstem so that the vertebral and basilar arteries were visible. The dura and arachnoid membranes were removed followed by continuous perfusion of the ventral medullary surface with 95% O_2/5% CO_2 equilibrated aCSF solution at 37 ± 0.5°C. The hypoglossal nerve (XII) and cervical vagus nerve (cVN) were isolated, cut, and their activity was measured using a suction electrode containing aCSF. Signals were amplified, bandpass filtered (8 Hz to 3 kHz), and digitized with a Digidata 1400 and pClamp 10 software (Molecular Devices).

After completion of the surgery, mice were allowed to stabilize for 15 min prior to obtaining 15–20 min of baseline respiratory activity. Using the vertebral and basilar arteries as landmarks (Fig. 3a–c), 200 μm diameter optical fibers coupled to a 447 nm DPSSL Driver lasers at (intensity < 230 mW/mm^2) were placed bilaterally on the ventral surface of the medulla above the region containing PiCo. XII and cVN activity were recorded during 10 second episode files containing a 200 ms light pulse to stimulate *Chat*-cre;Ai27 expressing cells. Inspiratory and postinspiratory (spontaneous or light-evoked) activity was analyzed using Clampfit 10 software (Molecular Devices). The phase of evoked cVN postinspiratory activity was determined as the fraction of the inspiratory cycle (Extended Data Fig. 9) or the fraction of the average duration of the preceding two inspiratory cycles (“expected phase”, Fig. 3e). The inspiratory phase duration during cycles containing a light-evoked PiCo burst were then divided by the expected phase to determine the “phase-delay” (Fig. 3e). In some mice, PiCo was photo-stimulated before and after bilateral injection of 5 μM DAMGO to assess the effect of DAMGO on the inspiratory phase-delay (Extended Data Fig. 10).

To test whether PiCo activity is necessary for postinspiration in vivo, pulled micropipettes containing somatostatin (SST; 750 μM) or DAMGO (5 μM), and either Evan’s Blue or Fast Green to identify the injection site, were inserted (300–400 μm) bilaterally into PiCo. Spontaneous postinspiratory burst amplitude, duration, and frequency were then quantified 3–5 min following a 250 nL injection of either SST or DAMGO and compared (student’s t-test) to pre-injection values (GraphPad, Prism 5 software). Postinspiratory burst duration was determined by subtracting the duration of XII nerve inspiratory activity from the duration of the corresponding cVN burst. Postinspiratory amplitude was defined as the amplitude of cVN activity immediately following XII nerve inspiratory activity. Following experimental protocols mice were perfused with 4% paraformaldehyde (PFA), and brainstems were extracted and cryoprotected (30% sucrose in PBS). Brainstems were then serially sectioned to identify sites of injection.

Immunohistochemistry

200 μm rostral transverse slices from *Vglut2*-cre;Ai14 were fixed with 4% PFA for 1 hour and immunostained as whole-mounts. Slices were washed in PBST (0.1–0.5% Triton X-100), blocked with 10% donkey serum in PBST overnight at 4°C, incubated for 2–3 days in primary antibody in blocking solution at 4°C, washed in PBST, incubated in secondary antibody in blocking solution for 5–8 hr at room temperature, washed in PBST, counterstained with 0.01% DAPI (Life Technologies), and mounted in Fluoromount-G (SouthernBiotech). 40 μm sagittal sections from *Vglut2*-cre;Ai14 mice were also immunolabeled for quantification. Animals were transcardially perfused with 4% PFA, and brainstems were postfixed in 4% PFA overnight. Isolated brainstems were transferred through increasing sucrose gradients (10–30%), embedded in OCT compound (TissueTek), frozen, and cryosectioned. Immunohistochemical labeling followed the same protocol as for whole-mounts with shortened incubation times. Primary antibodies included anti-ChAT (1:100, AB144P, Millipore) and anti-Cre Recombinase (1:200, 908001, BioLegend). Secondary antibodies were Alexa Fluor 568- or 647-conjugated (1:250, Life Technologies). Maximum intensity projections of optical slice z-stacks were acquired using a Zeiss 710 Quasar 34-channel LSCM (Carl Zeiss). Cre-labeled images were despeckled for background noise reduction.

Cell Counting

Maximum intensity projections of 20x optical slice z-stacks were collected −40 to 360 μm medial to the medial end of NA. ChAT+ and Cre+ or tdTomato+ cells were counted within this area, with the exception of ChAT+ cells that clearly belonged to the NA or VII nucleus (distinctive due to location and large cell size). Counts from each hemisphere were averaged for individual animals. Counts in the rostrocaudal direction were taken from sagittal slices 40 to 280 μm medial to the medial end of NA, where PiCo cells are most abundant. ChAT+ and Cre+ or tdTomato+ were counted in 50 μm bins through the rostrocaudal extent and summed across the 240 μm span. For *in vivo* experiments, 50 μm serial transverse brainstem sections were cryopreserved and processed as described above. Sections were imaged through the region encompassing the injection site and noted for the presence of Evan's blue or Fast Green dye. *Chat*-cre;Ai27 expression identified the rostral end of the NA in order to quantify the rostrocaudal location of injection sites relative to NA. Anatomical diagrams and coordinates were based on the adult mouse brain atlas[31].

In situ hybridization

(P)8–11 animals were perfused with 4% PFA (0.1M sodium phosphate, pH 7.0), and brainstems were post-fixed in 4% PFA (0.1M sodium phosphate, pH 7.0) + 4% sucrose, overnight at 4°C. Isolated brainstems were submerged in 30% sucrose, embedded in OCT, frozen at −80°C, and cryosectioned at 20 μm. Prior to hybridization, sections were fixed with 4% PFA/DEPC-PBS, pH 7.0 at 4°C for 5 min, treated with Proteinase K (1 μg/mL) for 10 min at room temperature, fixed with 4% PFA/DEPC-PBS, pH 7.0 at 4°C for 5 min, and acetylation for 10 min at room temperature. DIG labeled *Vglut2*-Dig antisense RNA probe [306 bp fragment of *Vglut2* (1563–1869bp, XM_006540602)] was hybridized onto sections (0.8 μg/mL) at 42°C overnight. Following hybridization, sections were incubated with

RNase A (50 μg/mL, Invitrogen) for 30 min at 37°C. DIG Nucleic acid detection kit (Roche) was used for RNA probe detection. The sections were incubated in anti-Digoxigenin-AP conjugate (Roche Applied Science, sheep, 1:1000) for 1 hr at room temperature. Hybridized molecules were visualized after incubation in an enzyme-catalyzed color reaction with a solution of 5-bromo-4-chloro-3-indolyl phosphate (BCIP) and nitroblue tetrazolium salt (NBT) (Roche Applied Science). The sections were developed in the BCIP/NBT solution for 2 hr in the dark at room temperature. The enzyme-catalyzed color reaction was stopped with TE, pH 8.0 and fixed in 4% PFA, pH 7.0 for 20 min at 4°C.

Statistics

All statistics were performed using GraphPad Prism 5. Numerical data are reported as the mean ± s.e.m. Normality was determined by D'Agostino-Pearson normality test. For normally distributed data, statistical significance was assessed by two-tailed paired Student's *t*-tests and two-way ANOVAs where appropriate. Two-way ANOVAs were followed by Bonferroni *post-hoc* correction. For data that were not normal, we used non-parametric two-tailed Mann Whitney, Kruskal-Wallis, one-way ANOVA, and repeated measures Friedman tests where appropriate. Kruskal-Wallis and Friedman tests were followed by Dunn's multiple comparison *post-hoc* tests. Variance was similar between groups that were statistically compared. Results were considered significant when $P < 0.05$. α was set less than or equal to 0.05 for multiple comparison tests. Sample sizes were chosen on the basis of previous studies.

Extended Data

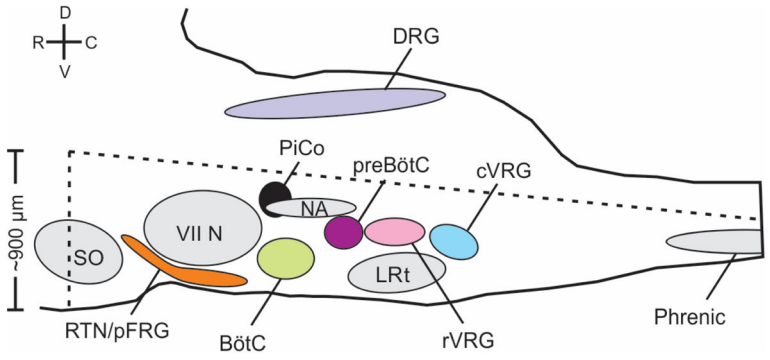

Extended Data Figure 1. Schematic of the horizontal slice from a sagittal view that retains the medullary ventral respiratory column in the brainstem

Dotted lines represent approximate boundaries of the horizontal slice. Slice retains part of the superior olive (SO), and the entire retrotrapezoidal nucleus/para-facial respiratory group (RTN/pFRG), facial nucleus (VII N), Bötzinger Complex (BötC), Post-inspiratory Complex (PiCo), Nucleus ambiguus (NA), preBötzinger Complex (preBötC), lateral reticular nucleus (LRT), and the rostral and caudal ventral respiratory groups (rVRG and cVRG, respectively). The slice also retains a portion of the spinal cord and includes part of the phrenic motor nucleus (approximately cervical segment 3 and 4). The slice does not contain the dorsal portion of the medulla including the dorsal respiratory group (DRG). Legend: dorsal (D), ventral (V), rostral (R), caudal (C).

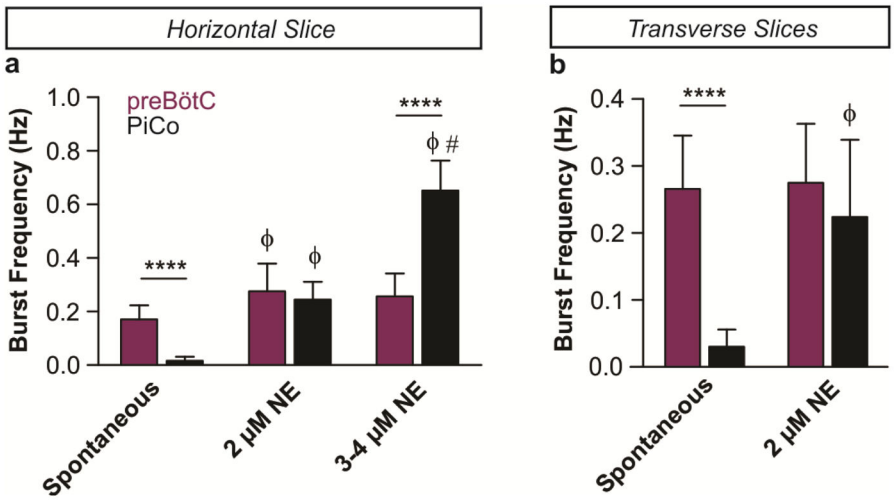

Extended Data Figure 2. NE dose response of preBötC and PiCo rhythms in horizontal and transverse slices

The frequency of the PiCo rhythm (black) is highly sensitive to the application of low concentrations of NE while the preBötC rhythm (purple) stays relatively constant in both types of slice preparations. **a,** In horizontal slices the PiCo rhythm is slow under spontaneous conditions (n=10), the two rhythms have similar burst frequencies in 2 µM NE (n=6), and the PiCo rhythm significantly outpaces the preBötC rhythm under higher concentrations (n=4, 3–4 µM NE). **b,** Similarly, when isolated in transverse slices, the PiCo rhythm has a slow frequency under spontaneous conditions (n=10), and the preBötC and PiCo have similar frequencies at 2 µM NE (n=7). (mean ± s.e.m.) Two-way ANOVA followed by a Bonferroni *post hoc* test. **** $P < 0.0001$ comparing PiCo to preBötC, ϕ $P<0.05$ compared to baseline (Spon.), # $P<0.05$ compared to 2 µM NE.

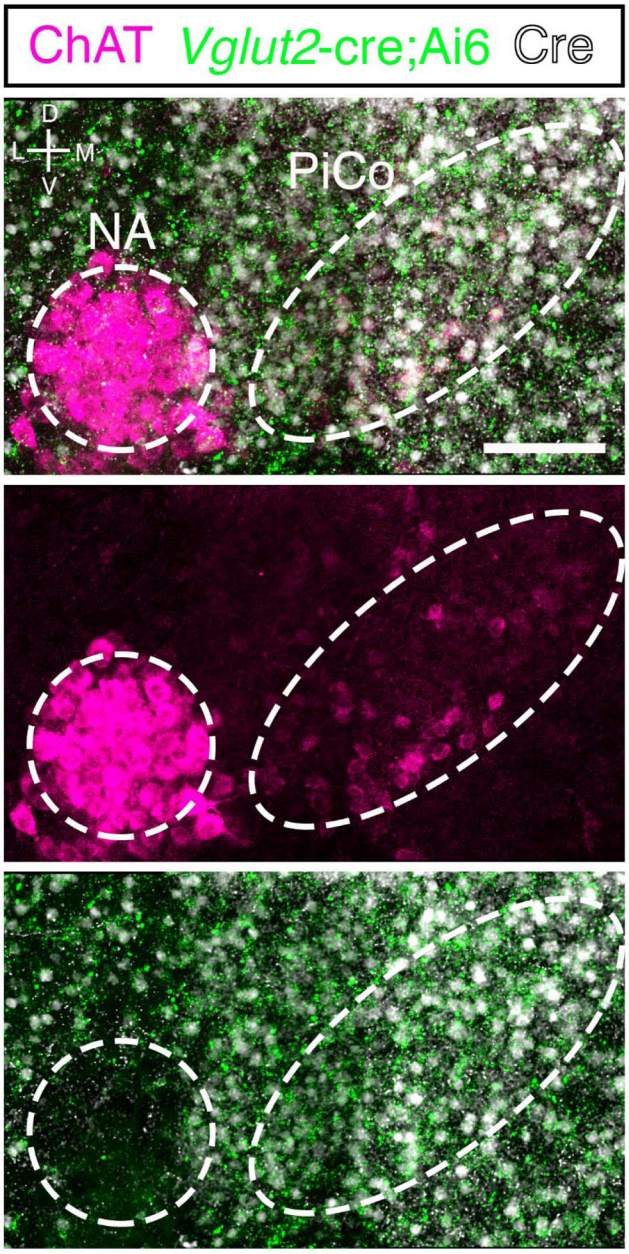

Extended Data Figure 3. NA neurons lack *Vglut2*-cre expression

High magnification view at the level of PiCo from a *Vglut2*-cre;Ai6 (ZsGreen1; green) mouse immunolabled with ChAT antibody (magenta) and Cre antibody (white). Note lack of green *Vglut2*-cre expression in the NA. Scale bar 100 μm.

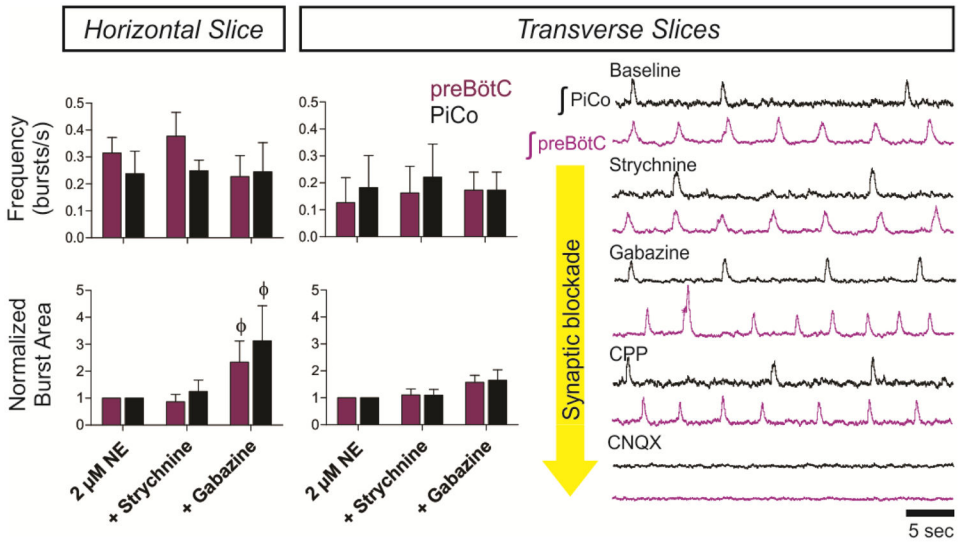

Extended Data Figure 4. Progressive synaptic blockade in horizontal and transverse slices

(Left) Graphs comparing frequency and normalized burst area between horizontal (n=5) and paired transverse slices (n=5) after the application of strychnine and gabazine. In both horizontal and paired transverse slices, PiCo and preBötC rhythms have nearly identical burst frequencies in the presence of gabazine (top graphs). The burst area of both rhythms also significantly increases with the application of gabazine in both slice preparations (bottom graphs). Two-way ANOVA followed by a Bonferroni *post hoc* test. ϕ $P<0.05$ compared to baseline (2 μM NE). (Right) Synaptic blockers were progressively perfused over paired transverse slices at 10 minute intervals. Both PiCo and preBötC rhythms persist in the presence of 1 μM strychnine, 10 μM gabazine, and 10 μM CPP. Population rhythms ceased in the presence of 20 μM CNQX, indicating that both rhythms are excitatory (n=5). The asterisk denotes a characteristic sigh in the preBötC trace.

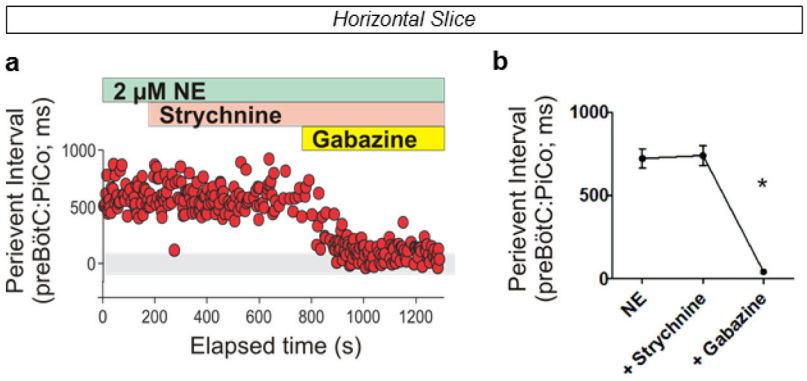

Extended Data Figure 5. Perievent interval between preBötC and PiCo bursts during inhibitory block in the horizontal slice

a, Peri-event interval, time between peak of preBötC and PiCo bursts, is constant in strychnine; however, gabazine initiates progressive synchronization between rhythms shown here in a representative experiment. **b,** Average peri-event intervals at baseline and after

sequential application of strychnine and gabazine (n=6, mean ± s.e.m.). Repeated measures Friedman test followed by Dunn's multiple comparisons *post-hoc* test. $*P < 0.05$.

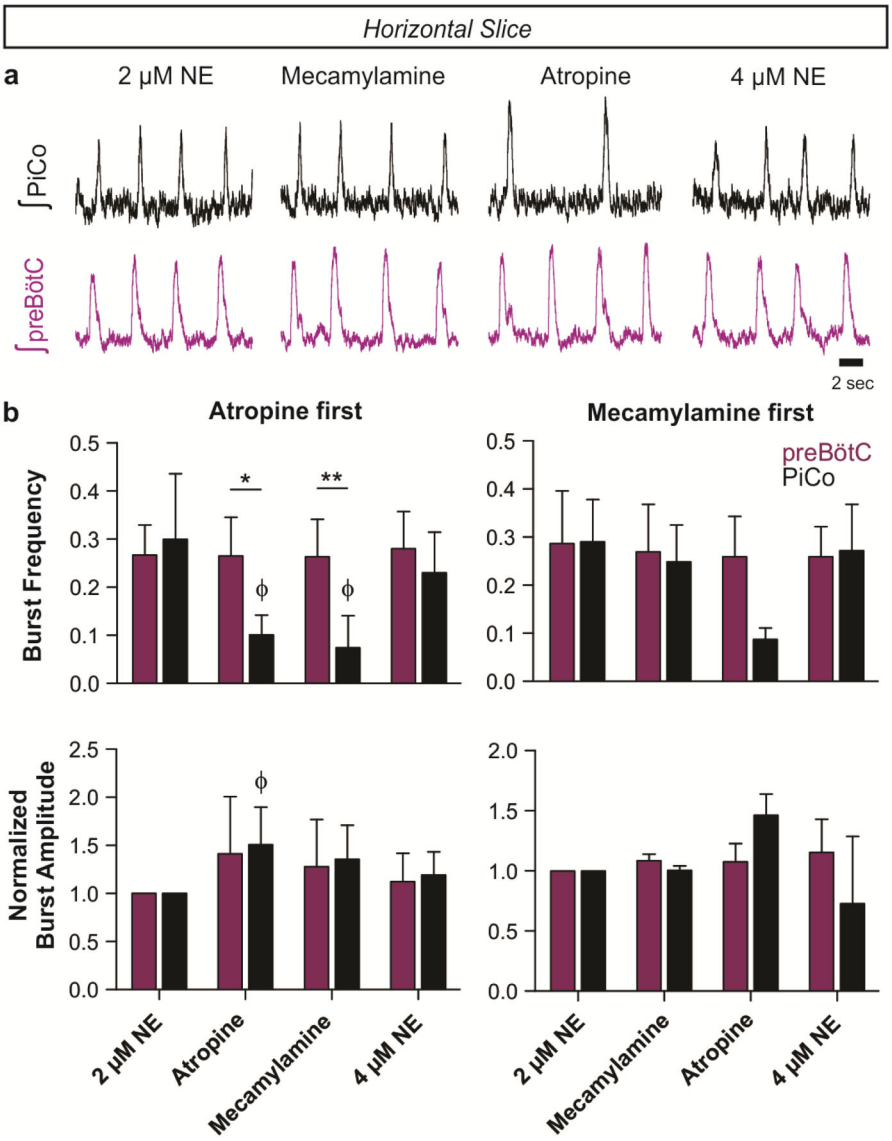

Extended Data Figure 6. Blocking muscarinic and nicotinic acetylcholine receptors does not abolish the PiCo rhythm

a, Raw population bursts from PiCo and contralateral preBötC with the progressive addition of 1 μM mecamylamine (nicotinic receptor antagonist), 10 μM atropine (muscarinic receptor antagonist), and 4 μM norepinephrine. **b,** The left two graphs show n=5 experiments in which atropine was applied first, and the right graphs illustrate n=3 experiments in which mecamylamine was applied first. Blockade of muscarinic receptors results in a larger decrease in PiCo burst frequency than blocking nicotinic receptors, while preBötC frequency does not change significantly (top graphs). Interestingly, blockade of muscarinic receptors increases the amplitude of PiCo bursts (bottom graphs). The PiCo rhythm persists after concurrent blockade of both types of acetylcholine receptors, and PiCo burst frequency

rebounds to near baseline levels when an additional 2 μM NE is applied (total 4 μM NE; top graphs). (mean ± s.e.m.). Two-way ANOVA followed by a Bonferroni *post hoc* test. ** $P <$ 0.01, * $P < 0.05$ comparing preBötC to PiCo, ϕ $P<0.05$ compared to baseline (2 μM NE).

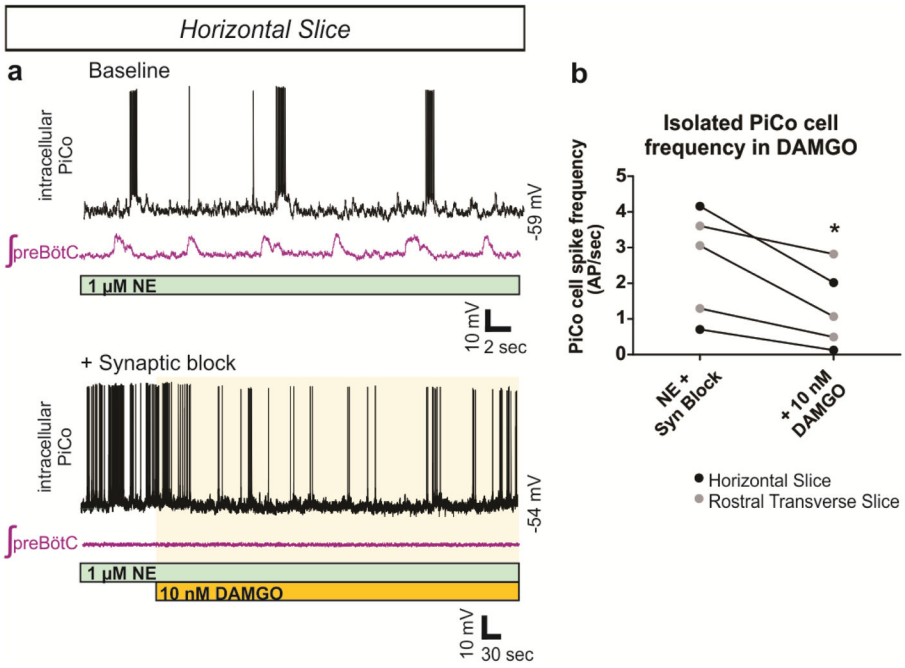

Extended Data Figure 7. Synaptically isolated PiCo neurons decrease firing frequency in the presence of DAMGO

a, Top traces show intracellular recordings from PiCo cells with concurrent extracellular preBötC population activity from a horizontal slice under 1 μM NE baseline conditions. Bottom traces show the same recordings after blocking fast synaptic transmission (1 μM strychnine, 10 μM gabazine, 10 μM CPP, 20 μM CNQX) to synaptically isolate the PiCo neuron. Application of 10 nM DAMGO decreases the cell's intrinsic firing frequency. **b**, Quantified data show that DAMGO significantly decreases action potential (AP) firing frequency of synaptically isolated PiCo neurons both in horizontal slices (black dots) and transverse PiCo slices (gray dots) (two-tailed paired *t*-test, * $P < 0.05$; n=5).

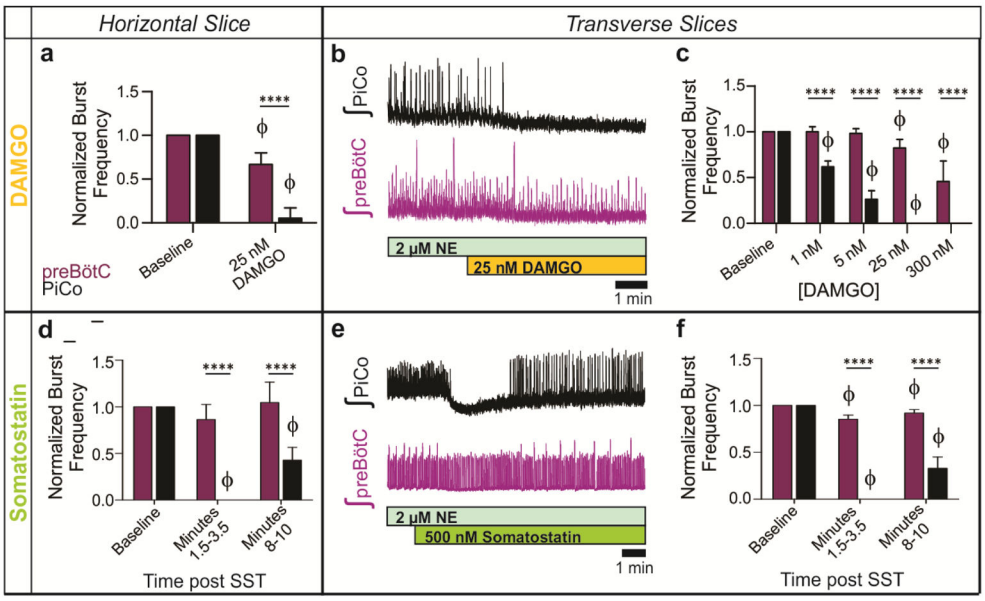

Extended Data Figure 8. Differential PiCo and preBötC population responses to DAMGO and SST in horizontal and transverse slices

a, After the application of 25 nM DAMGO, preBötC burst frequency only slightly decreases (n=5), whereas PiCo bursting is nearly eliminated. **b,** Similar to results observed in horizontal slices, the PiCo rhythm is eliminated by 25 nM DAMGO in transverse slices that isolate PiCo and preBötC in the presence of 2 µM NE (n=5). Periodic large amplitude bursts in the bottom preBötC trace are fictive sighs. **c,** DAMGO dose response of normalized preBötC and PiCo burst frequency in transverse slices, illustrating the differential sensitivity of the PiCo and preBötC rhythms to DAMGO; burst frequency values are normalized to baseline frequency in 2 µM NE. (mean ± s.e.m., n=8 with minimum replicates of 4 for each location and concentration). **d,** The PiCo rhythm is selectively and transiently inhibited by the application of 500 nM SST whereas the preBötC rhythm persists in horizontal slices. Graph shows normalized average burst frequencies of both rhythms at baseline, 1.5–3.5 minutes after SST application, and 8–10 minutes after SST application (n=6). **e,** Similar to the horizontal slice, SST application results in a robust inhibition of PiCo bursting in paired transverse slices. **f,** Similar to **d**, complied normalized burst frequencies for n=6 transverse slices before and after SST application. (mean ± s.e.m.) Two-way ANOVA followed by a Bonferroni *post hoc* test. ****$P < 0.0001$ comparing PiCo to preBötC, ϕ $P<0.05$ compared to baseline.

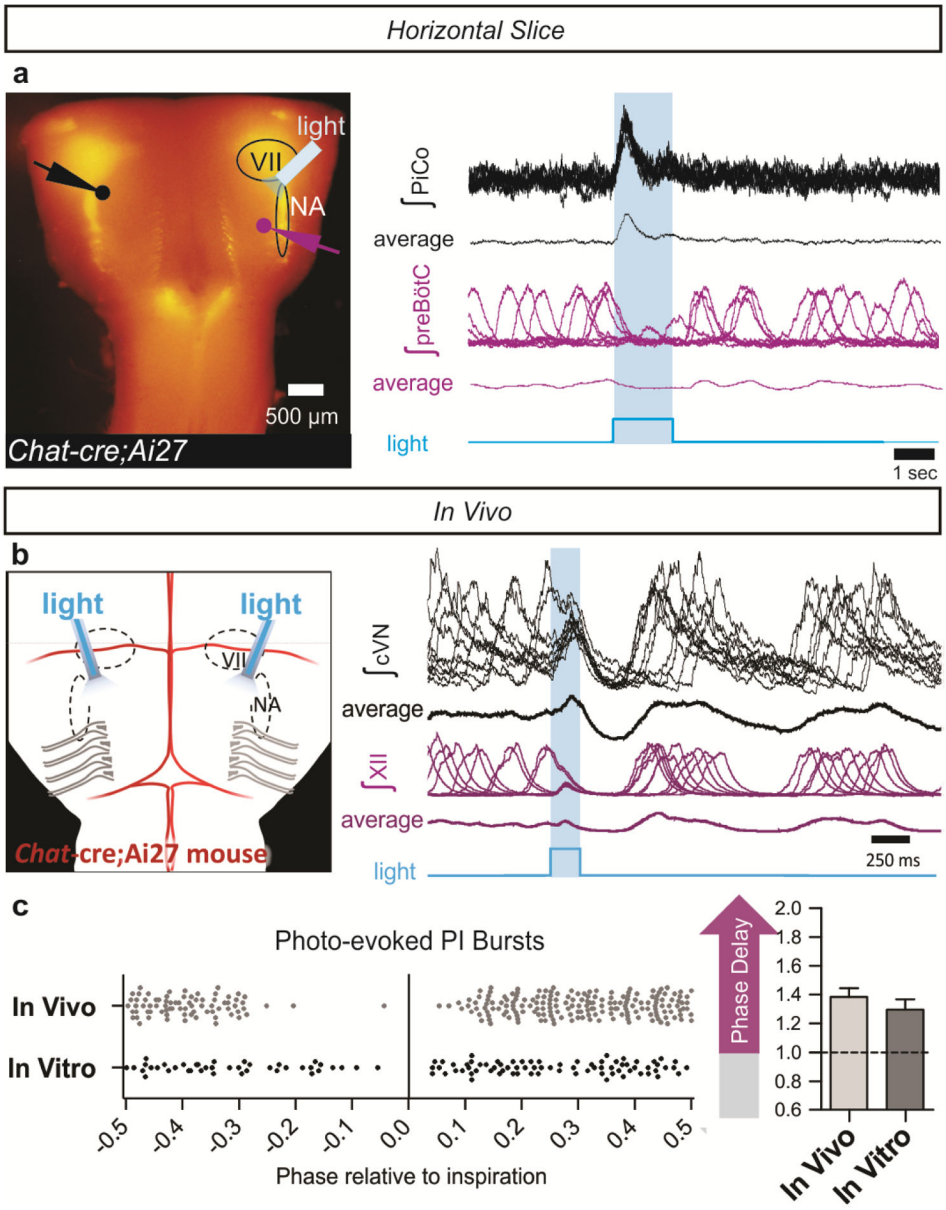

Extended Data Figure 9. Light stimulation of cholinergic cells evokes postinspiratory activity in horizontal slices and in vivo

a, Two population electrodes were placed at the level of PiCo (black dot and trace) and contralateral preBötC (purple dot and trace) in a *Chat*-cre;Ai27 horizontal slice. Under spontaneous conditions (no NE), cholinergic neurons expressing channelrhodopsin-2 were light activated with a fiber optic (labeled 'light') placed over PiCo ipsilateral to the preBötC electrode. PiCo population bursts were triggered upon the onset of a 1.5 second light pulse while no bursts were light evoked in the preBötC (n=6). Figure shows 10 traces overlaid for each electrode with averaged traces below from a representative experiment. **b,** Photo-stimulating PiCo in adult anesthetized *Chat*-cre;Ai27 mice reliably triggers cVN bursts. Figure shows 10 traces overlaid with averages below of cVN and XII activity during a 200 ms light stimulation of PiCo. **c**, Postinspiratory bursts can be photo-evoked both in vivo

(n=6) and in vitro (n=6) at any phase except for during inspiration and just prior to inspiration (bottom left) due to the inspiratory phase delay that occurs when PiCo is stimulated (mean ± s.e.m., bottom right). NA= Nucleus ambiguus, VII= facial nucleus.

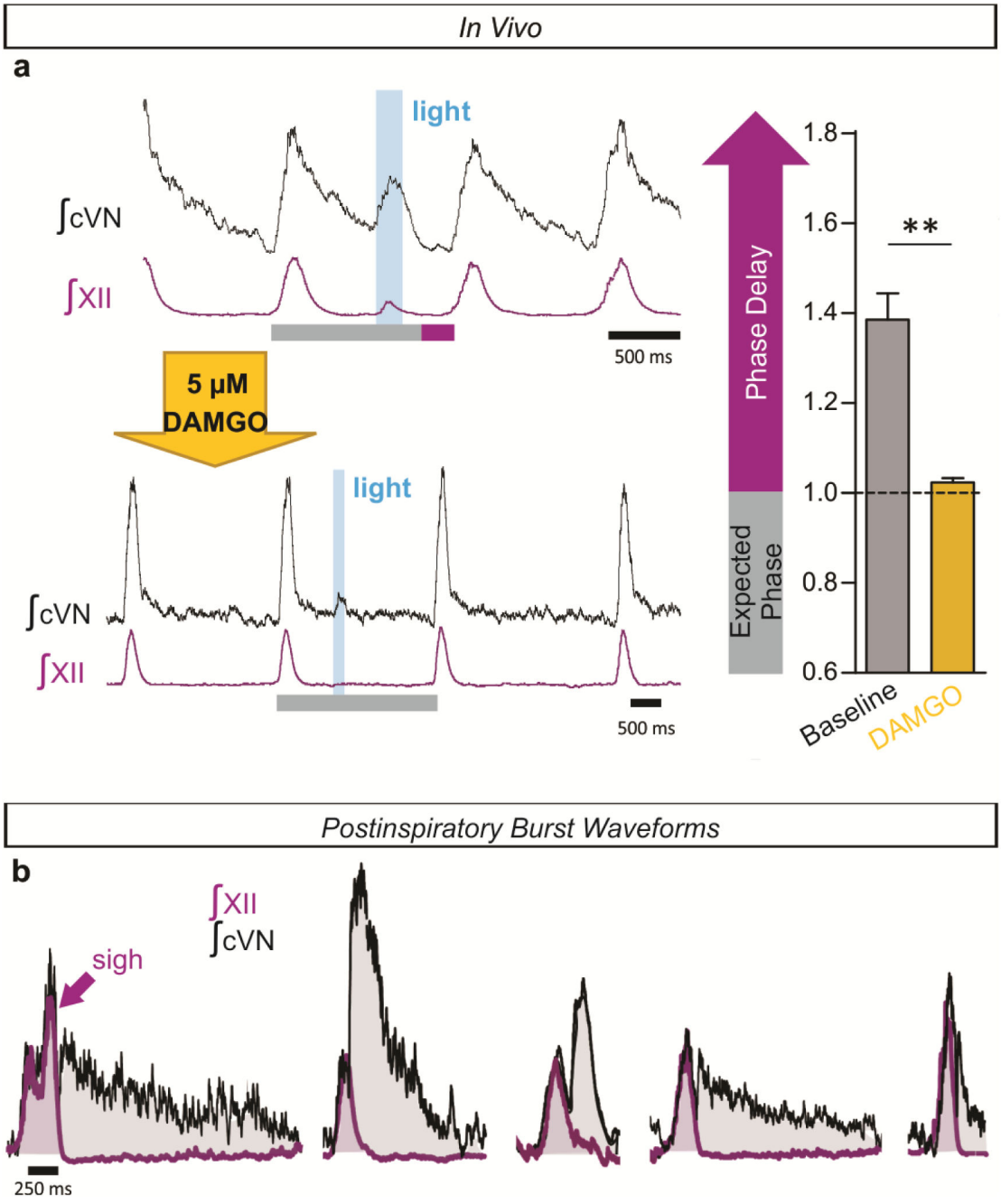

Extended Data Figure 10. Elimination of phase delay by DAMGO and a diversity of postinspiratory waveforms in vivo

a, Injection of 5 μM DAMGO into PiCo eliminates the phase delay elicited by photostimulation of PiCo in *Chat*-cre;Ai27 mice. A representative experiment showing cVN and XII recordings during a 200 ms light pulse before and after injection of PiCo with

DAMGO (left; gray bars = expected phase, purple bars = inspiratory phase delay) and the average inspiratory phase delay (right) (mean ± s.e.m., two-tailed paired t-test, **P<0.01; n=6). **b,** A diversity of postinspiratory vagal waveforms were recorded in vivo. Five examples of cVN (black) and XII (purple) recordings (overlaid) show that postinspiratory activity can vary from large decrementing patterns to small short bursts, potentially representing the neural basis for a variety of postinspiratory behaviors.

Acknowledgments

Supported by grants from the National Institute of Health NS087828-01 (awarded to T.A.), HL090554 (awarded to J-M.R.), and HL126523-01 (awarded to J-M.R.). The authors declare no conflicts of interest. We thank Paul Gray for constructive insights provided throughout the preparation of this manuscript, Tatiana Dashevskiy for creating the heat map of postinspiratory activity, Francesco Bodogni for obtaining in situ hybridization reagents, and Katie Cuthill for cryosectioning. J-MR would also like to thank DW Richter and SW Schwarzacher for their inspiration to study postinspiration.

References

1. Richter DW, Smith JC. Respiratory rhythm generation in vivo. Physiology (Bethesda). 2014; 29:58–71. DOI: 10.1152/physiol.00035.2013 [PubMed: 24382872]
2. Troche MS, Brandimore AE, Godoy J, Hegland KW. A framework for understanding shared substrates of airway protection. J Appl Oral Sci. 2014; 22:251–260. [PubMed: 25141195]
3. Smith JC, Ellenberger HH, Ballanyi K, Richter DW, Feldman JL. Pre-Botzinger complex: a brainstem region that may generate respiratory rhythm in mammals. Science (New York, NY). 1991; 254:726–729.
4. Huckstepp RT, Cardoza KP, Henderson LE, Feldman JL. Role of parafacial nuclei in control of breathing in adult rats. J Neurosci. 2015; 35:1052–1067. DOI: 10.1523/JNEUROSCI.2953-14.2015 [PubMed: 25609622]
5. Pagliardini S, et al. Active expiration induced by excitation of ventral medulla in adult anesthetized rats. J Neurosci. 2011; 31:2895–2905. DOI: 10.1523/JNEUROSCI.5338-10.2011 [PubMed: 21414911]
6. Smith JC, Abdala AP, Rybak IA, Paton JF. Structural and functional architecture of respiratory networks in the mammalian brainstem. Philos Trans R Soc Lond B Biol Sci. 2009; 364:2577–2587. DOI: 10.1098/rstb.2009.0081 [PubMed: 19651658]
7. Smith JC, Abdala AP, Koizumi H, Rybak IA, Paton JF. Spatial and functional architecture of the mammalian brain stem respiratory network: a hierarchy of three oscillatory mechanisms. Journal of neurophysiology. 2007; 98:3370–3387. 00985.2007 [pii]. DOI: 10.1152/jn.00985.2007 [PubMed: 17913982]
8. Alheid GF, McCrimmon DR. The chemical neuroanatomy of breathing. Respir Physiol Neurobiol. 2008; 164:3–11. DOI: 10.1016/j.resp.2008.07.014 [PubMed: 18706532]
9. Ruangkittisakul A, Kottick A, Picardo MC, Ballanyi K, Del Negro CA. Identification of the pre-Botzinger complex inspiratory center in calibrated “sandwich” slices from newborn mice with fluorescent Dbx1 interneurons. Physiol Rep. 2014; 2
10. Tan W, et al. Silencing preBotzinger complex somatostatin-expressing neurons induces persistent apnea in awake rat. Nature neuroscience. 2008; 11:538–540. DOI: 10.1038/nn.2104 [PubMed: 18391943]
11. Lieske SP, Thoby-Brisson M, Telgkamp P, Ramirez JM. Reconfiguration of the neural network controlling multiple breathing patterns: eupnea, sighs and gasps [see comment]. Nature neuroscience. 2000; 3:600–607. [PubMed: 10816317]
12. Hilaire G, Viemari JC, Coulon P, Simonneau M, Bevengut M. Modulation of the respiratory rhythm generator by the pontine noradrenergic A5 and A6 groups in rodents. Respir Physiol Neurobiol. 2004; 143:187–197. DOI: 10.1016/j.resp.2004.04.016 [PubMed: 15519555]
13. Madisen L, et al. A toolbox of Cre-dependent optogenetic transgenic mice for light-induced activation and silencing. Nature neuroscience. 2012; 15:793–802. [PubMed: 22446880]

14. Onimaru H, Arata A, Homma I. Firing properties of respiratory rhythm generating neurons in the absence of synaptic transmission in rat medulla in vitro. Exp Brain Res. 1989; 76:530–536. [PubMed: 2551710]
15. Gray PA, et al. Developmental origin of preBotzinger complex respiratory neurons. J Neurosci. 2010; 30:14883–14895. DOI: 10.1523/jneurosci.4031-10.2010 [PubMed: 21048147]
16. Janczewski WA, Feldman JL. Distinct rhythm generators for inspiration and expiration in the juvenile rat. J Physiol. 2006; 570:407–420. DOI: 10.1113/jphysiol.2005.098848 [PubMed: 16293645]
17. Burke PG, Abbott SB, McMullan S, Goodchild AK, Pilowsky PM. Somatostatin selectively ablates post-inspiratory activity after injection into the Botzinger complex. Neuroscience. 2010; 167:528–539. DOI: 10.1016/j.neuroscience.2010.01.065 [PubMed: 20149846]
18. Dutschmann M, Herbert H. The Kolliker-Fuse nucleus gates the postinspiratory phase of the respiratory cycle to control inspiratory off-switch and upper airway resistance in rat. The European journal of neuroscience. 2006; 24:1071–1084. DOI: 10.1111/j.1460-9568.2006.04981.x [PubMed: 16930433]
19. Subramanian HH, Holstege G. Midbrain and medullary control of postinspiratory activity of the crural and costal diaphragm in vivo. Journal of neurophysiology. 2011; 105:2852–2862. DOI: 10.1152/jn.00168.2011 [PubMed: 21451058]
20. Grillner S. The motor infrastructure: from ion channels to neuronal networks. Nature reviews. Neuroscience. 2003; 4:573–586. DOI: 10.1038/nrn1137 [PubMed: 12838332]
21. Kiehn O. Locomotor circuits in the mammalian spinal cord. Annual review of neuroscience. 2006; 29:279–306. DOI: 10.1146/annurev.neuro.29.051605.112910
22. Stein PS. Neuronal control of turtle hindlimb motor rhythms. Journal of comparative physiology. A, Neuroethology, sensory, neural, and behavioral physiology. 2005; 191:213–229. DOI: 10.1007/s00359-004-0568-6
23. Wiggin TD, Anderson TM, Eian J, Peck JH, Masino MA. Episodic swimming in the larval zebrafish is generated by a spatially distributed spinal network with modular functional organization. Journal of neurophysiology. 2012; 108:925–934. DOI: 10.1152/jn.00233.2012 [PubMed: 22572943]
24. Evans JA, Elliott JA, Gorman MR. Dynamic interactions between coupled oscillators within the hamster circadian pacemaker. Behavioral neuroscience. 2010; 124:87–96. DOI: 10.1037/a0018088 [PubMed: 20141283]
25. Hill AA, Garcia AJ 3rd, Zanella S, Upadhyaya R, Ramirez JM. Graded reductions in oxygenation evoke graded reconfiguration of the isolated respiratory network. Journal of neurophysiology. 2011; 105:625–639. [PubMed: 21084689]
26. Doi A, Ramirez JM. State-dependent interactions between excitatory neuromodulators in the neuronal control of breathing. J Neurosci. 2010; 30:8251–8262. 30/24/8251 [pii]. DOI: 10.1523/JNEUROSCI.5361-09.2010 [PubMed: 20554877]
27. Madisen L, et al. A robust and high-throughput Cre reporting and characterization system for the whole mouse brain. Nature neuroscience. 2010; 13:133–140. DOI: 10.1038/nn.2467 [PubMed: 20023653]
28. Hirata T, et al. Identification of distinct telencephalic progenitor pools for neuronal diversity in the amygdala. Nature neuroscience. 2009; 12:141–149. DOI: 10.1038/nn.2241 [PubMed: 19136974]
29. Telgkamp P, Cao YQ, Basbaum AI, Ramirez JM. Long-term deprivation of substance P in PPT-A mutant mice alters the anoxic response of the isolated respiratory network. Journal of neurophysiology. 2002; 88:206–213. [PubMed: 12091546]
30. Franklin, K., Paxinos, G. The Mouse Brain in Stereotaxic Coordinates. 3. Academic Press; 2008.

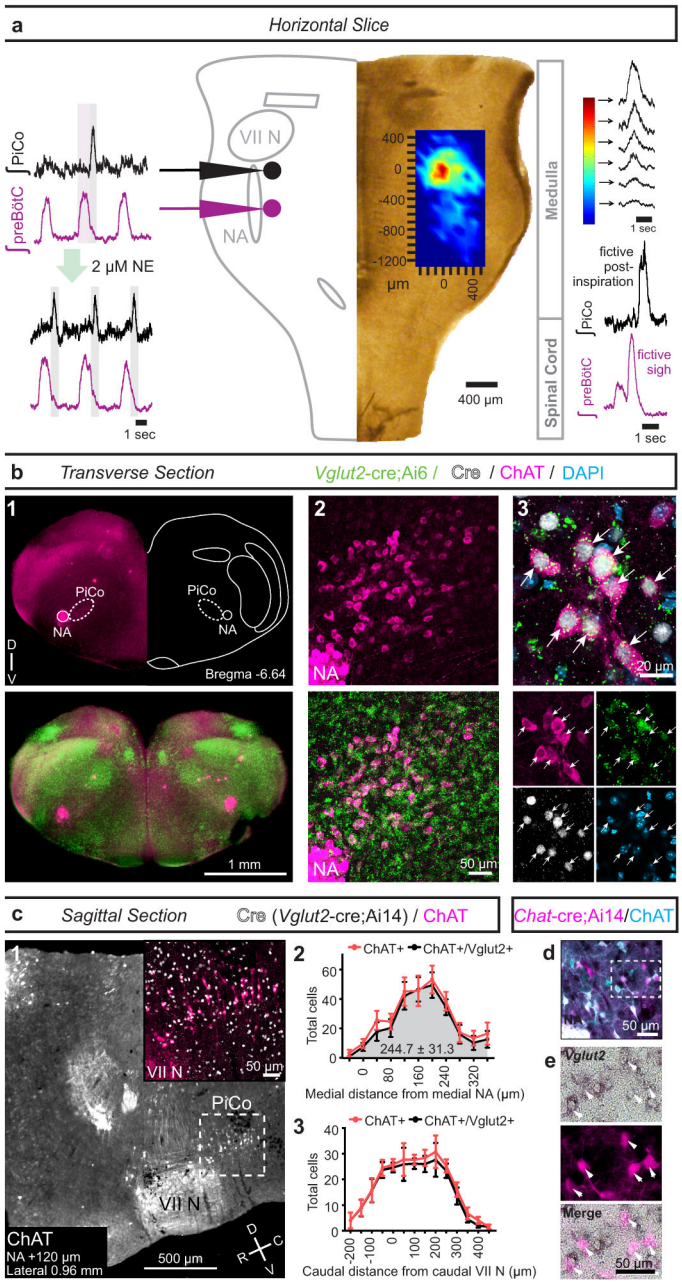

Figure 1. Horizontal slice and anatomy of PiCo

a, Population bursts PiCo (black), preBötC (purple). 2 μM NE stimulates PiCo bursts (n=23). Left, schematic; right, heat map of PiCo burst amplitude; legend (n=6). PiCo bursts follow fictive sighs. **b1,** Immunohistochemical labeling of PiCo dorsomedial to NA. **b2,** Higher magnification ChAT, *Vglut2*-cre;Ai6 (ZsGreen1) colocalization within PiCo. **b3,** Arrows: higher magnification triple-labeled ChAT+ ZsGreen1+ Cre+ PiCo cells (n=5). **c1,** Sagittal view, ChAT+ PiCo neurons (dashed-box). Inset, magnified dashed-box, colocalization of ChAT+, Cre+ PiCo neurons in *Vglut2*-cre;Ai14 mice. **c2,3,** Quantification of ChAT- and Vglut2-expressing PiCo cells mediolaterally from NA (244.7±31.3 average

total # cells; n=5) **c2,** and rostrocaudally from VII N (n=4) **c3,** Bars, mean ± sem. **d,** ChAT+ PiCo neurons, *Chat*-cre;Ai14 mice. **e,** Magnified box (**d)** Arrowheads, *Vglut2* mRNA in *Chat*-derived PiCo neurons.

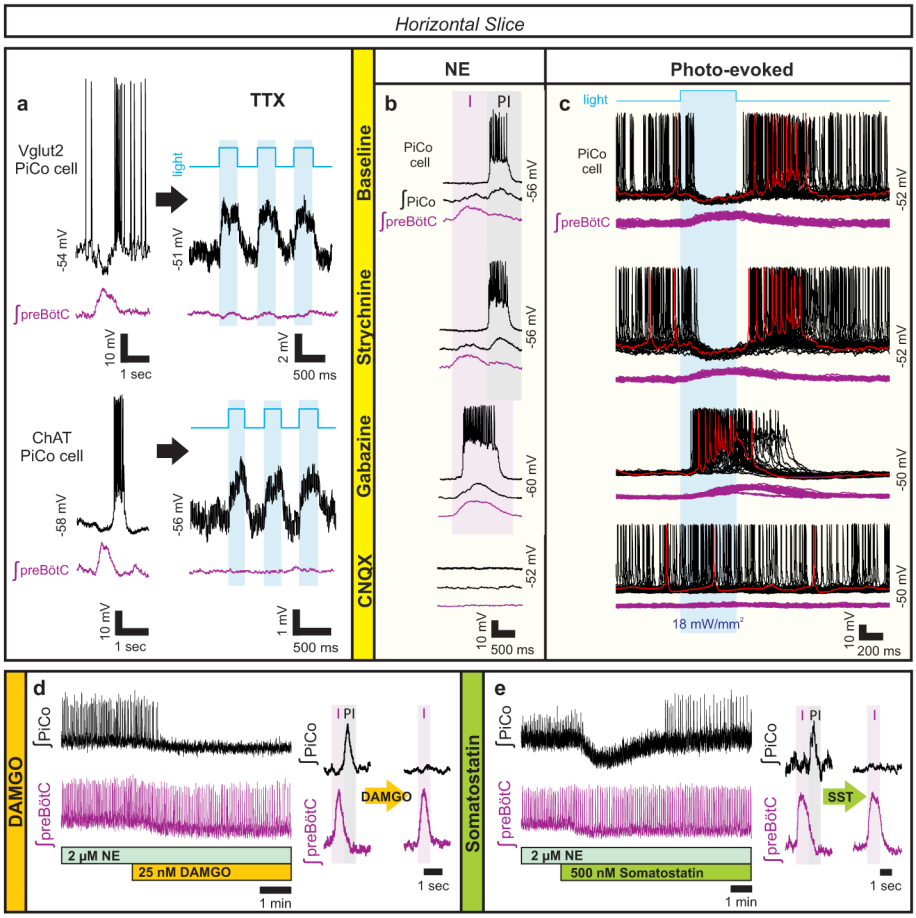

Figure 2. Glutamatergic, cholinergic PiCo cells and role of synaptic inhibition

a, Intracellular PiCo recordings in *Vglut2*-cre;Ai27 (n=3) and *Chat*-cre;Ai27 (n=5) horizontal slices. Photo-stimulation after TTX depolarizes membrane potential. **b,** PiCo, preBötC in progressive synaptic block (n=5). Rhythms synchronized in gabazine, bursting abolished in CNQX. **c,** PiCo cell in *Dbx1*-cre;Ai27 horizontal slice with progressive synaptic block. PiCo cell inhibited during photo-evoked inspiratory burst in NE/strychnine, bursts with light-stimulation in gabazine, ceases bursting in CNQX (500 ms light, 40 sweeps, n=4). **d,** PiCo bursting eliminated by 25 nM DAMGO; representative bursts (n=5). **e,** PiCo inhibited by 500 nM SST; representative bursts (n=6).

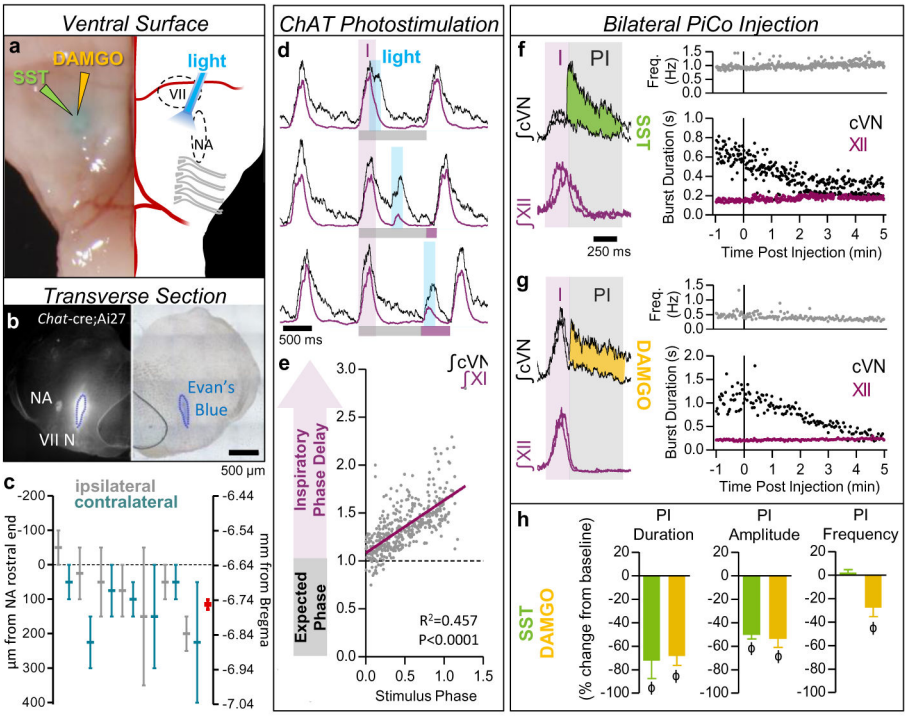

Figure 3. Stimulation and inhibition of PiCo in vivo

a, Left, brightfield image; right, schematic; ventral sites for bilateral photo-stimulation, injection of SST/DAMGO in vivo. **b,** Representative dye injection at PiCo level. Left, *Chat*-cre;Ai27; right, brightfield. **c,** Dye-spread (n=7), centered at PiCo (0–200 µm caudal from rostral NA). Ipsilateral (grey), contralateral (teal) injections, bars ±max/min; pooled data in red, mean ± s.e.m. **d**, PiCo photo-stimulation in adult *Chat*-cre;Ai27 mice evokes vagal bursts and delays subsequent inspiration (grey bars = expected inspiratory phase, purple bars = inspiratory phase delay) **e**, Quantification of inspiratory phase delay (n=6); magnitude dependent on stimulus phase (slope: 0.549, linear regression analysis). **f,g,** Injection of SST or DAMGO progressively decreases cVN, not XII burst duration. **h,** Postinspiratory burst duration, amplitude, and frequency following injection of SST (n=3), DAMGO (n=4). Two-tailed paired t-test, ϕ $P<0.05$ compared to baseline; mean ± s.e.m.

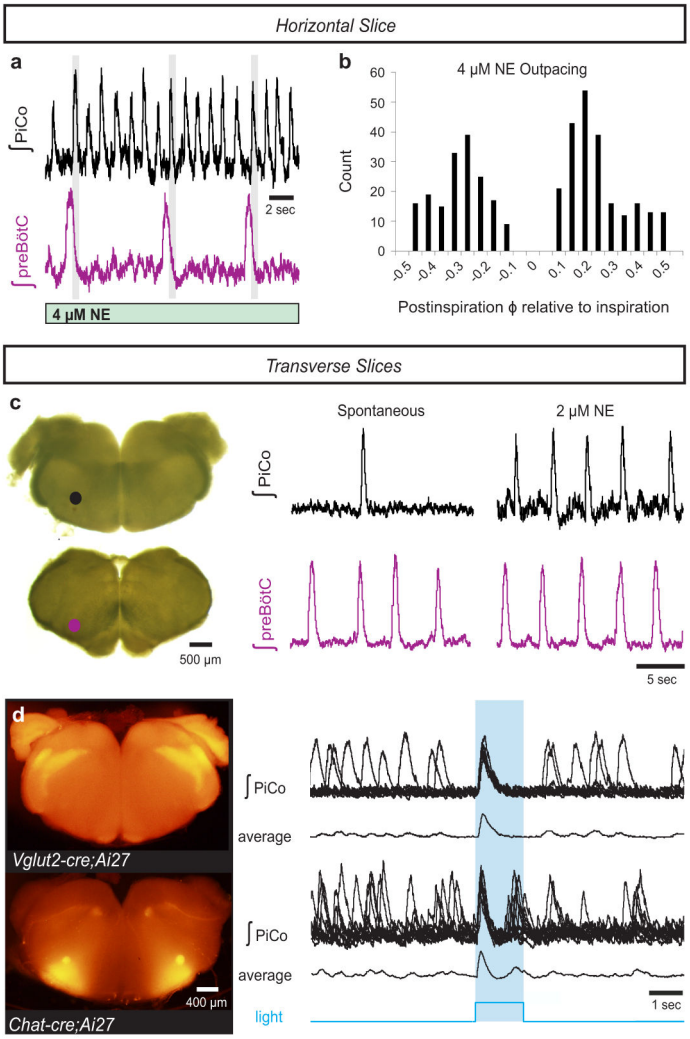

Figure 4. PiCo is an autonomous, rhythm generating network

a, In 3–4 µM NE, PiCo outpaces the preBötC rhythm, but still bursts in the postinspiratory phase (gray bars) in horizontal slices. **b,** PiCo bursts occur in any phase except during inspiration (inspiratory peak=0; count=400 bursts; n=4). **c,** PiCo and preBötC isolated in transverse in vitro slices; PiCo bursting stimulated by 2 µM NE (n=33). **d,** Light stimulation evokes a burst in *Vglut2*-cre;Ai27 rostral transverse slices (91.3 ± 5.1% of stimulations, mean ± s.e.m., n=4) and *Chat*-cre;Ai27 slices (91.9 ± 1.8% of stimulations, mean ± s.e.m., n=6). 1.5 second light pulse. Top traces: 10 sweep overlay, bottom traces: sweep average.